journal

J. Am. Ceram. Soc., **83** [10] 2572–83 (2000)

The Wulff Shape of Alumina: II, Experimental Measurements of Pore Shape Evolution Rates

Mikito Kitayama,*,† Takayuki Narushima,*,‡ and Andreas M. Glaeser*

Department of Materials Science and Engineering, University of California, Berkeley, California 94720

Lawrence Berkeley National Laboratory, Berkeley, California 94720

Department of Materials Science and Engineering, Massachusetts Institute of Technology, Cambridge, Massachusetts 02139

The rate at which a facetted tetragonal cavity of nonequilibrium shape approaches a cubic equilibrium (Wulff) shape via surface diffusion was modeled. The shape relaxation rate of a facetted "stretched cylinder" was also modeled. For the first geometry, only an approximate solution based on linearizing the mean potential difference between the source and sink facets was obtained. For the stretched cylinder, both an approximate and an exact solution can be obtained; the approximate solution underestimates the evolution rate by a factor of ≈2. To assess the applicability of the models, nonequilibrium shape pores of identical initial geometry (≈20 μm × 20 μm × 0.5 μm) were introduced into (0001), {10$\bar{1}$2}, {11$\bar{2}$0}, and {10$\bar{1}$0} surfaces of sapphire single crystals using microfabrication techniques, ion-beam etching, and hot pressing. The large (≈20 μm × 20 μm) faces of the pore are low-index surfaces whose nature is dictated by the wafer orientation. A series of anneals was performed at 1900°C, and the approach of the pore shape to an equilibrium shape was monitored. The kinetics of shape evolution are highly sensitive to the crystallographic orientation and stability of the low-index surface that dominates the initial pore shape. The measured variations of the pore aspect ratio were compared to those predicted by the kinetic model. The observations suggest that when the initial bounding surface is unstable, shape relaxation may be controlled by diffusion. However, surface-attachment-limited kinetics (SALK) appears to play a major role in determining the pore shape evolution rate in cases where the initial bounding surfaces have orientations that are part of the Wulff shape.

I. Introduction

THE rate of microstructural changes resulting from the displacement of crystal interfaces can be limited either by the rate at which mass diffuses from a source to a sink or by the rate at which mass is accommodated at the sink or released at the source. The surface or interface structure will determine the density and nature of sites at which atom addition or removal can occur, and thereby, the maximum mass arrival or removal rate that can be accommodated. A low site density is expected for coherent grain boundaries, and for surfaces that are facetted. For facetted surfaces, atomic-height ledges/steps that provide preferred addition/removal sites can arise either due to physical imperfections in the surface (e.g., scratches), structural imperfections in the crystal (e.g., a screw dislocation), or due to a disparity between the macroscopic surface orientation and the orientation of the facet (a "miscut"). When the initial ledge density is low, or ledges are progressively removed, the rate of microstructural change in facetted systems may ultimately depend upon the rate at which critical-size atomic-height patches of atoms (or atomic-depth cavities) can form by nucleation on the migrating facet. In this paper, the term surface-attachment-limited kinetics (SALK) is used to describe cases where *any* of the spectrum of interfacial processes limits the rate of microstructural change. Ideally, it would be of interest to determine which specific interfacial process yields interfacial-reaction-rate-limited evolution or SALK. A more modest goal is to determine the conditions under which SALK impacts the rate of microstructural change.

Recently, two approaches to modeling surface-diffusion-controlled shape changes of fully facetted 2-D features[1,2] were used to predict pore shape change rates in alumina.[3,4] The first,[2] an approximate approach, assumes that the mass flux across a specific facet edge is proportional to the difference in the *mean* potentials on the adjoining facets scaled by an appropriate transport distance. The facet displacement rate is dictated by the total mass (volume) arrival rate and the facet area. The second, more refined approach stipulates that the divergence of the flux must be constant everywhere on a facet in order for the facet to advance or recede uniformly, and calculates the spatial variation of the potential on the facet consistent with this requirement and other boundary conditions.[1] In a prior paper,[4] the predictions of these two 2-D models are shown to agree to within a factor of 1.5 when consistent values of materials parameters are used, and modeling errors are corrected.[§] Comparison of the (2-D model) predictions[4] with the results of experimental work[3] examining discrete, i.e., 3-D, features suggested that observed evolution rates were influenced by interfacial reaction rates (SALK) and not limited by the rate of surface diffusion.

The present paper addresses this issue by extending the modeling from 2-D to 3-D geometries, introducing an experimental technique that provides for more controlled study of pore shape evolution, and comparing the observed evolution characteristics with those predicted for surface-diffusion-controlled evolution.

Predictions of the rate of shape change of discrete facetted features based on linearizing the potential difference between adjacent facets are presented. Where possible, the predictions of this approximate approach are compared to those of the more exact approach. The validity of using a 2-D model to interpret 3-D evolution characteristics is assessed.

C. A. Handwerker—contributing editor

Manuscript 189425. Received April 12, 1999; approved May 17, 2000.

*Member, American Ceramic Society. This research was supported by the Director, Office of Energy Research, Office of Basic Energy Sciences, Materials Sciences Division of the U.S. Department of Energy, under Contract No. DE-AC03-76SF00098.

†Now at Functional Materials Engineering, Fukuoka Institute of Technology, 3-30-1 Wajiro-Higashi, Higashi-ku, Fukuoka 811-0295, Japan.

‡Now at Department of Metallurgy, Tohoku University, Aza Aoba, Aramaki, Aoba-ku, Sendai 980-8579, Japan.

§The nature of the errors and inconsistencies are discussed in Ref. 4. A short note providing further detail is also in preparation.

The experimental study exploits methods[5] applied in prior model experiments examining microstructural evolution in ceramics, and the high-temperature properties of surfaces and interfaces in alumina.[5–13] The sequential application of microlithographic techniques, ion beam etching, and hot pressing to sapphire substrates of controlled surface orientation can yield intragranular arrays of pores of controlled size and shape. The pores have much greater lateral (parallel to the original surface) extent than depth. By systematically varying the substrate orientation, internal cavities of identical shape but bounded in large part by different crystallographic planes of sapphire can be produced. When samples containing these (highly) nonequilibrium shape pores are annealed, the resulting shape change rates will depend upon whether the process is rate-limited by diffusion or dictated by SALK. Since sapphire is transparent, shape changes can be tracked (nondestructively) by optical microscopy, and the effect of the orientation of the dominant bounding surface on the evolution rates can be assessed. After annealing is complete, the pores can be exposed by polishing; this procedure is simplified because the processing leads to planar arrays of pores. Since the substrate surface orientation and directions within the surface are known, scanning electron microscopy (SEM) and the atomic force microscope (AFM) can be used to characterize the cavity geometry and index the facets that formed during annealing. This information provides some insight as to the nature of the stable surfaces under the annealing conditions, and is helpful in interpreting the kinetic observations.

The comparison of model predictions and experimental results suggests that although shape relaxation may initially be controlled by diffusion, SALK plays a major role in determining the pore shape evolution rate when the dominant initial bounding surfaces are part of the Wulff shape. The results of the present study also proved useful in guiding the design of experiments aimed at determining the Wulff shape of doped and undoped aluminas. The results of these studies will be reported separately.[14–16]

II. Modeling of Pore Shape Changes

This section addresses surface-diffusion-controlled pore shape changes. Two geometries are considered. The first is that of a facetted tetragonal pore that relaxes to a cubic equilibrium shape; this shape change approaches that in the experiments performed. However, for this shape, only an approximate solution is possible. As a result, we also consider the relaxation of a coin-shaped pore to a more equiaxed cylindrical "plug". For this geometry, both an exact solution based on a position-dependent potential, and an approximate solution based on linearizing the difference in mean potentials on adjoining surfaces, can be obtained. The results show that, as in the 2-D cases considered previously,[4] the difference between these solutions is small.

(1) Analysis of a Stretched Cube

The geometry of interest is that of a particle (or cavity) with dimensions $2l_2 \times 2l_2 \times 2l_1$, with l_2 initially much greater than l_1, as illustrated in Fig. 1. The volume of the particle V_p is conserved during the shape change. All facets undergo uniform normal displacements, and the four facets of area $4l_1l_2$ are assumed to move at the same rate, so that the square cross section is conserved during the process. The surface energy of the two square facets of area $4l_2^2$, and normal to l_1, is denoted γ_1. These square facets are referred to as Type I facets. The surface energy of the four facets of area $4l_1l_2$ is denoted γ_2. These four facets are subsequently referred to as Type 2 facets.

Proceeding in a manner analogous to that used in the companion paper,[4] we develop expressions for the driving force for mass flow and link the driving force to a rate of shape change. The volume conservation condition, $V_p = 8l_1l_2^2 = \text{constant}$, relates the normal displacements of the Type I and Type 2 facets

$$dl_1 = -\frac{2l_1}{l_2}\,\mathrm{d}l_2 \tag{1}$$

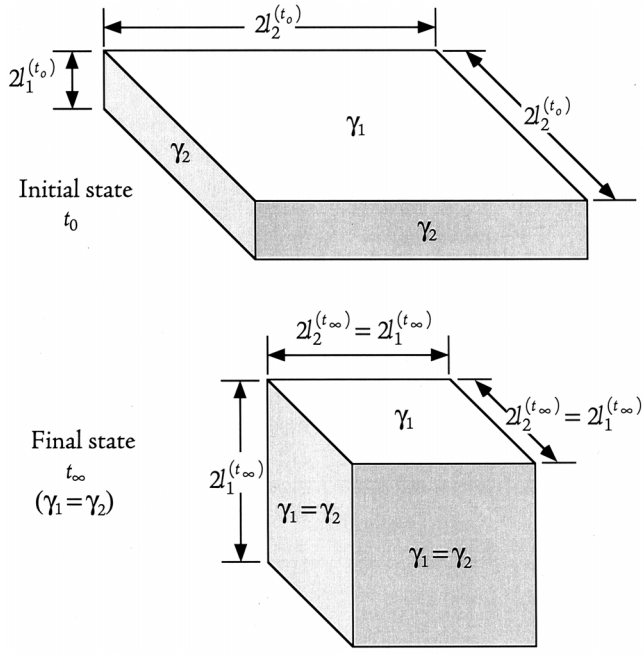

Fig. 1. Illustration of geometry and parameters used in modeling a "stretched cube."

When $\gamma_1 = \gamma_2 = \gamma$, and the equilibrium shape is a cube, the more general expression for the change in the total surface energy of the particle/cavity reduces to

$$(\mathrm{d}\Phi)_{\text{total}} = 8\left(\gamma_2 l_2 - \gamma_1 \frac{l_2^2}{l_1}\right)\mathrm{d}l_1 = 8\gamma l_2\left(1 - \frac{l_2}{l_1}\right)\mathrm{d}l_1 \tag{2}$$

When $l_2 > l_1$, the energy change is negative when $\mathrm{d}l_1 > 0$; the driving force goes to zero when $l_1 = l_2$. Equating the total volume swept when the two Type I facets each undergo a displacement $\mathrm{d}l_1$, $8l_2^2\mathrm{d}l_1$, to the product of the number of moles transferred dn and the molar volume, $\bar{V}$, and substituting into Eq. (2), yields the differential free energy change

$$(\mathrm{d}\Phi)_{2\to1} = \gamma\bar{V}\left(\frac{1}{l_2} - \frac{1}{l_1}\right)\mathrm{d}n \tag{3}$$

The ratio of $(\mathrm{d}\Phi)_{2\to1}$ and dn defines a chemical potential difference, and thus,

$$\frac{(\mathrm{d}\Phi)_{2\to1}}{\mathrm{d}n} = \Delta\bar{\mu}_{2\to1} = \bar{\mu}_1 - \bar{\mu}_2 = \gamma\bar{V}\left(\frac{1}{l_2} - \frac{1}{l_1}\right) \tag{4}$$

The identical result can be obtained using the concept of weighted mean curvature (wmc).[17] The displacement of a facet of Type I by an amount δl_1 extends all four of the orthogonal Type 2 facets, and increases the area of each by $2l_2{\cdot}\delta l_1$. The total surface energy change is thus $8l_2\gamma_2{\cdot}\delta l_1$. The volume swept by the displacement is $4l_2^2{\cdot}\delta l_1$. The wmc of facet 1 is simply the limit of the energy change per volume swept as the volume swept goes to zero, and is thus given by

$$\text{wmc}_1 = \frac{8l_2\gamma_2 \cdot \delta l_1}{4l_2^2 \cdot \delta l_1} = \frac{2\gamma_2}{l_2} \tag{5}$$

A displacement of a Type 2 facet extends surfaces of both Type I and Type 2. The total surface area and total surface energy changes for the Type I facets due to a displacement of a single Type 2 facet by δl_2 are $2{\cdot}2l_2{\cdot}\delta l_2$ and $4l_2\gamma_1{\cdot}\delta l_2$, respectively. The extension of the two adjoining Type 2 facets contributes surface area and surface energy changes of $2{\cdot}2l_1{\cdot}\delta l_2$, and $4l_1\gamma_2{\cdot}\delta l_2$, respectively. The volume swept by the displacement is $2l_1{\cdot}2l_2{\cdot}\delta l_2$. Thus,

$$\mathrm{wmc}_2 = \frac{4(l_2\gamma_1 + l_1\gamma_2){\cdot}\delta l_2}{4l_1l_2{\cdot}\delta l_2} = \frac{\gamma_1}{l_1} + \frac{\gamma_2}{l_2} \tag{6}$$

Converting to chemical potentials, and evaluating $\Delta\bar{\mu}_{2\rightarrow1}$

$$\Delta\bar{\mu}_{2\rightarrow1} = \bar{\mu}_1 - \bar{\mu}_2 = [\mu_0 + \bar{V}(\mathrm{wmc}_1)] - [\mu_0 + \bar{V}(\mathrm{wmc}_2)] = \bar{V}\left(\frac{\gamma_2}{l_2} - \frac{\gamma_1}{l_1}\right) \tag{7}$$

which reduces to Eq. (4) when $\gamma_1 = \gamma_2 = \gamma$.

To develop a differential equation for the shape change rate, we again set the total mass arrival rate on a Type I facet equal to the sum of the mass arrival rates at the facet edges. As before,[4] these flow rates are dictated by the potential gradients at the facet edges. If we implicitly assume that the deposition rate is uniform on the facet, the problem of determining the shape change rate reduces to one of calculating or estimating the gradients at the facet edges. We apply the equation

$$(J_s)_{2\rightarrow1} = -\frac{D_s}{\bar{V}kT}\frac{\Delta\bar{\mu}_{2\rightarrow1}}{\Delta x_{2\rightarrow1}} \tag{8}$$

with $\Delta\bar{\mu}_{2\rightarrow1} = \bar{\mu}_1 - \bar{\mu}_2$ equal to the difference in mean potential, Eq. (7), and $\Delta x_{2\rightarrow1}$ approximated as $\frac{1}{2}(l_1 + l_2)$ to estimate the edge flux. The choice of $\Delta x_{2\rightarrow1}$ reflects the approximate distance between points on the adjoining facets at which the linearly varying potential equals the mean potential. The volume swept by a facet of Type I with area A_1 $(= 4l_2^2)$, is denoted $\mathrm{d}V_1$, and related to the surface flux via

$$\mathrm{d}V_1 = A_1\delta l_1 = J_s{\cdot}\delta_s{\cdot}L{\cdot}\Omega\cdot\mathrm{d}t \tag{9}$$

where δ_s is the diffusion width or surface thickness, taken here to be equal to $\Omega^{1/3}$ where Ω is the atomic volume, and L is the total common or shared edge length between the interacting facets. Rearranging the result, substituting Eqs. (7) and (8), and setting $\gamma_1 = \gamma_2 = \gamma$ gives

$$\frac{\mathrm{d}l_1}{\mathrm{d}t} = \frac{2\Omega^{4/3}}{l_2}{\cdot}J_s = -\frac{32D_s\gamma\Omega^{4/3}}{V_pkT}\left[\frac{l_1 - l_2}{l_1 + l_2}\right] \tag{10}$$

For the stretched cube, with l_2 set equal to $(V_p/8l_1)^{1/2}$, one can solve for $\mathrm{d}t$ and integrate. This leads to

$$(t - t_0)_{\mathrm{StrCube}} = -\int_{l_1^{(t_0)}}^{l_1^{(t)}} \frac{V_pkT}{32D_s\gamma\Omega^{4/3}}\left[\frac{2\sqrt{2}l_1^{3/2} + \sqrt{V_p}}{2\sqrt{2}l_1^{3/2} - \sqrt{V_p}}\right]\mathrm{d}l_1 \tag{11}$$

Two solutions of different form can be obtained. The first is expressed in terms of a hypergeometric function, ${}_2F_1$, and has the form

$$(t - t_0)_{\mathrm{StrCube}} = -\frac{V_pkT}{16D_s\gamma\Omega^{4/3}}\left\{\frac{1}{2}(l_1^{(t)} - l_1^{(t_0)}) - \left(l_1^{(t)}{\cdot}{}_2F_1\left[\frac{2}{3}, 1, \frac{5}{3}, \frac{2\sqrt{2}{\cdot}(l_1^{(t)})^{3/2}}{\sqrt{V_p}}\right] - l_1^{(t_0)}{\cdot}{}_2F_1\left[\frac{2}{3}, 1, \frac{5}{3}, \frac{2\sqrt{2}{\cdot}(l_1^{(t_0)})^{3/2}}{\sqrt{V_p}}\right]\right)\right\} \tag{12}$$

The second solution is given in Eq. (13).

$$\begin{aligned}(t - t_0)_{\mathrm{StrCube}} = {} & -\frac{V_pkT}{32D_s\gamma\Omega^{4/3}}(l_1^{(t)} - l_1^{(t_0)}) \\ & - \frac{V_p^{1/3}kT}{24D_s\gamma\Omega^{4/3}}\left[\frac{V_p}{4}\ln\frac{\left[l_1^{(t)} - \left(\frac{1}{2}V_p^{1/3}\right)\right]\left[l_1^{(t)1/2} - \left(\frac{1}{2}V_p^{1/3}\right)^{1/2}\right]\left[l_1^{(t_0)1/2} + \left(\frac{1}{2}V_p^{1/3}\right)^{1/2}\right]}{\left[l_1^{(t_0)} - \left(\frac{1}{2}V_p^{1/3}\right)\right]\left[l_1^{(t_0)1/2} - \left(\frac{1}{2}V_p^{1/3}\right)^{1/2}\right]\left[l_1^{(t)1/2} + \left(\frac{1}{2}V_p^{1/3}\right)^{1/2}\right]}\right. \\ & + \frac{V_p}{8}\ln\frac{\left[l_1^{(t_0)2} + l_1^{(t_0)}\left(\frac{1}{2}V_p^{1/3}\right) + \left(\frac{1}{2}V_p^{1/3}\right)^2\right]\left[l_1^{(t_0)} + \left(\frac{1}{2}l_1^{(t_0)}V_p^{1/3}\right)^{1/2} + \frac{1}{2}V_p^{1/3}\right]\left[l_1^{(t)} - \left(\frac{1}{2}l_1^{(t)}V_p^{1/3}\right)^{1/2} + \frac{1}{2}V_p^{1/3}\right]}{\left[l_1^{(t)2} + l_1^{(t)}\left(\frac{1}{2}V_p^{1/3}\right) + \left(\frac{1}{2}V_p^{1/3}\right)^2\right]\left[l_1^{(t)} + \left(\frac{1}{2}l_1^{(t)}V_p^{1/3}\right)^{1/2} + \frac{1}{2}V_p^{1/3}\right]\left[l_1^{(t_0)} - \left(\frac{1}{2}l_1^{(t_0)}V_p^{1/3}\right)^{1/2} + \frac{1}{2}V_p^{1/3}\right]} \\ & + \frac{\sqrt{3}V_p}{4}\left(\arctan\left[\frac{1}{\sqrt{3}}\left(\frac{4l_1^{(t_0)}}{V_p^{1/3}} + 1\right)\right] - \arctan\left[\frac{1}{\sqrt{3}}\left(\frac{4l_1^{(t)}}{V_p^{1/3}} + 1\right)\right] + \arctan\left\{\frac{1}{\sqrt{3}}\left[\left(\frac{8l_1^{(t)}}{V_p^{1/3}}\right)^{1/2} + 1\right]\right\}\right. \\ & \left.\left. - \arctan\left\{\frac{1}{\sqrt{3}}\left[\left(\frac{8l_1^{(t_0)}}{V_p^{1/3}}\right)^{1/2} + 1\right]\right\} + \arctan\left\{\frac{1}{\sqrt{3}}\left[\left(\frac{8l_1^{(t)}}{V_p^{1/3}}\right)^{1/2} - 1\right]\right\} - \arctan\left\{\frac{1}{\sqrt{3}}\left[\left(\frac{8l_1^{(t_0)}}{V_p^{1/3}}\right)^{1/2} - 1\right]\right\}\right)\right]\end{aligned} \tag{13}$$

(2) Comparison with 2-D Simulation

Prior 2-D modeling[4] considered the rate at which a pore of rectangular cross section and constant area A_{cs} in the x–y plane, and infinite extent in the z-direction, would adjust its shape by surface diffusion. In the 3-D case, the areas of all bounding facets change during

evolution; volume is conserved. As a result, the evolution characteristics in 2-D and 3-D differ. Choi *et al.*[3] show that discrete submicrometer size pores of nonequilibrium shape persist in sapphire after 50 h anneals at 1600°C; the 2-D analysis[4] predicts that pores of such size should have a shape indistinguishable from the equilibrium shape after only a few minutes. The results of the 3-D analysis, Eqs. (12) and (13), can be compared to their 2-D analogues[4] to assess whether this is possibly a consequence of using a 2-D model to interpret kinetic data from discrete 3-D cavities. Since Choi *et al.*[3] generated pores by crack healing, and the initial pore geometries are not known, quantitative comparisons will assume an initial pore geometry matching that used in the experimental phase of the present study. Specifically, the cavities are assumed to be 20 μm × 20 μm × 0.5 μm. With $2l_1 = 0.5$ μm, and $2l_2 = 20$ μm, $A_{cs} = 4l_1l_2 = 10^{-11}$ m^2, $V_p = 8l_1l_2^2 = 2 \times 10^{-16}$ m^3, and the initial width-to-depth or aspect ratio R_a ($=2l_2/2l_1$) is 40.

Both the 2-D and 3-D solutions are derived by integrating an equation of the form

$$\frac{dl_1}{dt} = \frac{J_s \cdot \delta_s \cdot L \cdot \Omega}{A_1} = \frac{\Omega^{4/3} \cdot L}{A_1}\left(-\frac{D_s}{\bar{V}kT}\right)\left(\frac{\Delta\bar{\mu}_{2\to1}}{\Delta x_{2\to1}}\right) \quad (14)$$

With $\gamma_1 = \gamma_2 = \gamma$, it follows that in both cases, the time required to reach a given aspect ratio R_a from a common initial value at some fixed temperature will be proportional to $kT/D_s\gamma\Omega^{4/3}$. Thus, the *ratio* of the times required for a given aspect ratio change at fixed temperature will be independent of the specific values of D_s and γ assumed. The time ratio will instead depend upon the relative values of the chemical potential gradient, the relative edge lengths across which mass flows onto the facet, and the relative displacements that lead to a given change in aspect ratio.

At the onset of evolution, the chemical potential gradient for the 2-D and 3-D cases are identical, and thus, differences in evolution rates reflect differences in the factor L. Initially, facets of Type I in the 3-D stretched cube have twice the edge length of the 2-D stretched square, and thus twice the mass arrival rate; it follows that initially $(dl_1/dt)_{3D} = 2(dl_1/dt)_{2D}$. However, the aspect ratio of the stretched cube does not change at twice that of the stretched square because the facet displacements required to achieve a given change of aspect ratio differ in the two cases. This can be seen by expressing l_1 in terms of R_a for both the 2-D and 3-D cases

$$l_1^{2D} = \left(\frac{A_{cs}}{4R_a}\right)^{1/2} \quad (15a)$$

$$l_1^{3D} = \left(\frac{V_p}{8R_a^2}\right)^{1/3} \quad (15b)$$

The dependence of l_1 on R_a for the initial geometry of interest is shown in Fig. 2. Except at the initial point, $l_1^{2D} \neq l_1^{3D}$, and the facet displacements for a given change of aspect ratio, Δl_1^{2D} and Δl_1^{3D}, are also not equal. For small displacements, the differences are more easily seen by examining the ratio of the displacements, also

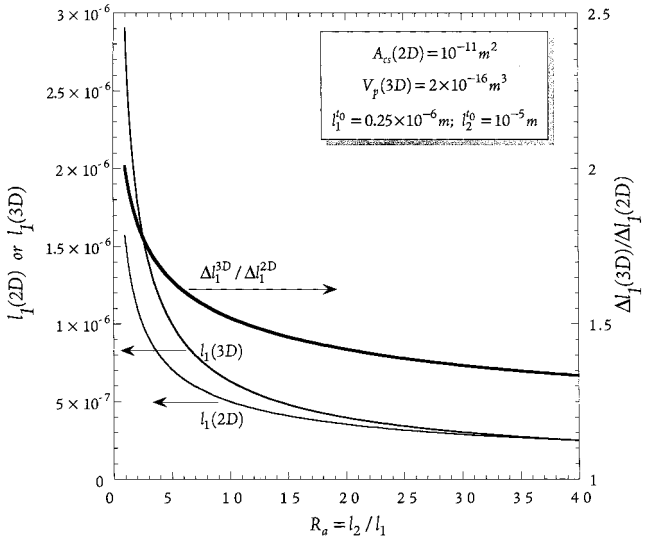

Fig. 2. Comparison of the aspect ratio (R_a) dependence of length l_1 for the case of a 2-D and a 3-D cavity or particle of indicated cross sectional area and volume. The ratio of the displacements of the facet necessary to achieve a given value of R_a is also plotted.

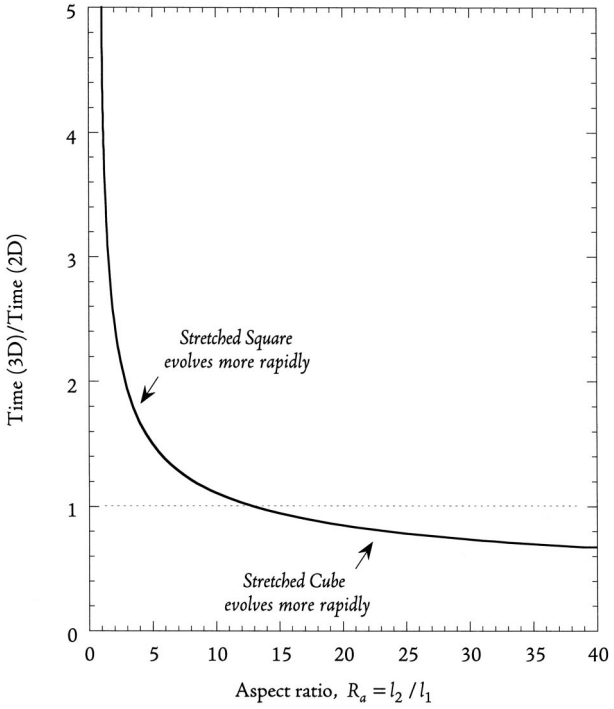

Fig. 3. Plot of the evolution time ratio, comparing the evolution of a stretched cube and a stretched square.

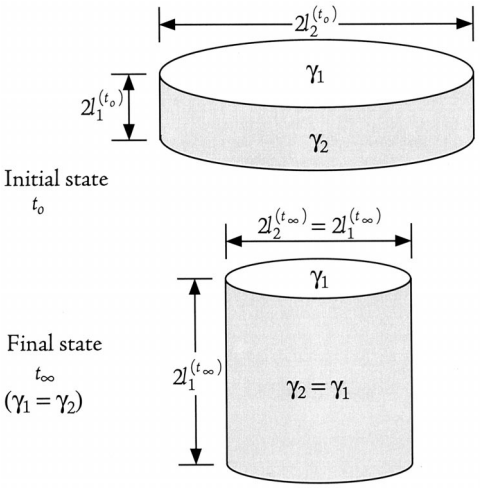

Fig. 4. Illustration of geometry and parameters used in modeling a "stretched cylinder."

plotted in Fig. 2. The ratio of $\Delta l_1^{3D}/\Delta l_1^{2D}$ approaches 1.33 when R_a approaches the initial value of 40.¶ Although the total displacement is thus larger for the 3-D case, this is offset by the greater edge length, and thus one expects that during the early stages of evolution, the time ratio, t_{3D}/t_{2D}, for small changes of aspect ratio will approach 0.667. The stretched cube evolves more rapidly.

At later stages of evolution, the difference in the displacement requirements for specific aspect ratio changes, and the associated differences in the values of l_1 and l_2, have multiple effects on the relative evolution rates. For the 2-D case, the edge length L remains constant, while for the 3-D case it decreases with time. Although the expressions for $\Delta\bar{\mu}$ for the 3-D and 2-D cases have an identical functional form, Eq. (7), the comparison in Fig. 2 shows that the values of l_1 and l_2 differ at fixed R_a. As a result, $\Delta\bar{\mu}$ will *not* be the same at fixed R_a. This is apparent when $\Delta\bar{\mu}$ is expressed in terms of R_a, and the area conservation and volume conservation conditions are invoked, yielding

$$\Delta\bar{\mu} = \gamma\bar{V}\left(\frac{1}{l_2} - \frac{1}{l_1}\right) = \gamma\bar{V}(1 - R_a)\left(\frac{1}{l_2}\right) \tag{16a}$$

$$\Delta\bar{\mu} = \gamma\bar{V}(1 - R_a)\left(\frac{4l_1}{A_{cs}}\right) \qquad \text{(2-D case)} \tag{16b}$$

$$\Delta\bar{\mu} = \gamma\bar{V}(1 - R_a)\left(\frac{8l_1}{V_p}\right)^{1/2} \qquad \text{(3-D case)} \tag{16c}$$

The net effect of the decreasing value of L, the relatively lower and decreasing value of $\Delta\bar{\mu}$, and the relatively higher and increasing value of Δx for the 3-D case is that as R_a approaches the equilibrium value, the relative rates of evolution reverse, and the stretched square (2-D) ultimately evolves more rapidly. This is illustrated in Fig. 3. At aspect ratios near 40, the ratio $t_{3D}/t_{2D} \approx 0.67$, whereas when the aspect ratio is 1.01 (near the equilibrium value), $t_{3D}/t_{2D} \approx 5.5$. We note that until R_a becomes ≤ 3, the error is no more than a factor of 2. Although the 2-D analysis underestimates the evolution time required to reach a near-equilibrium value of R_a, the evolution rates suggested by the pore geometries in the study of Choi *et al.*[3] remain much lower than would be expected for surface-diffusion-controlled evolution.

(3) Analysis of a Coin-Shaped Cavity

We now consider the shape relaxation of a cylindrical disk, as illustrated in Fig. 4, to a more nearly equiaxed cylindrical plug. The radius of the cylinder is taken to be $r = l_2$, and the depth of the disk is taken to be $2l_1$. The aspect ratio, R_a, defined as the width w divided by the depth d, is thus again l_2/l_1. For the purpose of defining driving forces for the shape change, the surface energy of the large circular face of area A_1 is assumed to be γ_1, and that of the edge face is γ_2.

The calculation of the driving force for transfer of mass from the edge face to the circular face involves determining the mean chemical potential on the two surfaces. This can be done by differential geometry or by determining the weighted mean curvature of the mass sink (Face I) and the mass source (Face 2). In view of the equivalence of these approaches, we focus here on a treatment in terms of wmc.

Adding mass to the top face, Face I, extends the edge or perimeter face. If one adds volume $\pi r^2 \cdot \delta l_1 = \pi l_2^2 \cdot \delta l_1$ to Face I, the surface area of the edge face increases by $2\pi r \cdot \delta l_1 = 2\pi l_2 \cdot \delta l_1$, and the surface energy increase is $2\pi l_2 \cdot \gamma_2 \cdot \delta l_1$. The weighted mean curvature of Face I is therefore given by

$$\text{wmc}_1 = \frac{2\pi l_2 \cdot \gamma_2 \cdot \delta l_1}{\pi l_2^2 \cdot \delta l_1} = \frac{2\gamma_2}{l_2} \tag{17}$$

Adding mass to the edge face, Face 2, involves the extension of the top and bottom faces, and enlargement of the perimeter. If one adds volume $2l_1 \cdot 2\pi r \cdot \delta r = 4\pi l_1 l_2 \cdot \delta l_2$, both the top and bottom surfaces increase their area by $2\pi l_2 \cdot \delta l_2$, leading to a combined surface energy change of $4\pi l_2 \cdot \gamma_1 \cdot \delta l_2$. The area of the perimeter increases by $4\pi l_1 \cdot \delta l_2$ and the resulting surface energy change is $4\pi l_1 \cdot \gamma_2 \cdot \delta l_2$. As a result, the weighted mean curvature of Face 2 is

$$\text{wmc}_2 = \frac{4\pi l_2 \cdot \gamma_1 \cdot \delta l_2 + 4\pi l_1 \cdot \gamma_2 \cdot \delta l_2}{4\pi l_1 l_2 \cdot \delta l_2} = \frac{\gamma_1}{l_1} + \frac{\gamma_2}{l_2} \tag{18}$$

It follows that the driving force for mass transfer from Face 2 to Face I is given by

$$\begin{aligned}\Delta\bar{\mu}_{2\to1} &= \bar{\mu}_1 - \bar{\mu}_2 \\ &= [\mu_0 + \bar{V}(\text{wmc}_1)] - [\mu_0 + \bar{V}(\text{wmc}_2)] \\ &= \bar{V}\left(\frac{\gamma_2}{l_2} - \frac{\gamma_1}{l_1}\right)\end{aligned} \tag{19}$$

To develop a rate equation describing the shape change, we again apply Eq. (8) with $\Delta\bar{\mu}_{2\to1} = \bar{\mu}_1 - \bar{\mu}_2$ now defined by Eq. (19), and $\Delta x_{2\to1}$ again approximated as $\frac{1}{2}(l_1 + l_2)$ to determine the edge flux. With $\gamma_1 = \gamma_2 = \gamma$ the flux per unit edge length takes the form

$$(J_s)_{2\to1} = \frac{2D_s\gamma}{kT}\left[\frac{l_2 - l_1}{l_1 l_2 (l_1 + l_2)}\right] \tag{20}$$

For displacement of the circular face, the volume swept by the "top" face of area $A_1 (= \pi l_2^2)$ due to a displacement δl_1 is denoted dV_1, and related to the surface flux via

$$dV_1 = A_1 \delta l_1 = J_s \cdot \delta_s \cdot L \cdot \Omega \cdot dt \tag{21}$$

with L in this case being $2\pi l_2$. With these substitutions, rearrangement yields

$$\begin{aligned}\frac{dl_1}{dt} &= \left(\frac{2\Omega^{4/3}}{l_2}\right) J_s \\ &= \frac{4D_s\gamma\Omega^{4/3}}{kT}\frac{1}{l_2}\left[\frac{l_2 - l_1}{l_1 l_2 (l_1 + l_2)}\right] \\ &= \frac{8\pi D_s\gamma\Omega^{4/3}}{V_p kT}\left[\frac{l_2 - l_1}{(l_1 + l_2)}\right]\end{aligned} \tag{22}$$

The volume conservation condition, $V_p = \text{constant} = 2\pi l_2^2 l_1$ can be used to re-express l_2 in terms of V_p and l_1. Rearrangement then yields

$$(t - t_0)_{\text{StrCyl}} = \int_{l_1^{(t_0)}}^{l_1^{(t)}} \frac{V_p kT}{8\pi D_s\gamma\Omega^{4/3}}\left[\frac{\sqrt{V_p} + (2\pi l_1^3)^{1/2}}{\sqrt{V_p} - (2\pi l_1^3)^{1/2}}\right] dl_1 \tag{23}$$

The result is clearly similar to that given as Eq. (11), and will have a similar solution. Numerical differences will arise because of the difference in the numerical coefficient, and also because the difference in shape will lead to different values of l_1 relative to those for the stretched cube at identical values of R_a (see Eq. (24)). When the times required for a stretched cylinder and a stretched cube of equal volume and identical initial aspect ratio to evolve to a constant new value of R_a are compared, they are in a constant ratio of 1.38. This result can be obtained most readily by using

¶This limiting ratio of 4/3 is a consequence of the assumed geometry. This can be seen by evaluating dl_1/dR_a for both the 2-D and 3-D cases, and examining the ratio when R_a assumes its initial value. It follows that the ratio of the evolution times must also approach a limiting value of 2/3 as R_a approaches its initial value.

$$(t-t_0)_{\mathrm{StrCyl}} = -\frac{V_p kT}{8\pi D_s \gamma \Omega^{4/3}}\left(l_1^{(t)} - l_1^{(t_0)}\right)$$
$$-\frac{4^{1/3}V_p^{4/3}kT}{8\pi^{4/3}D_s\gamma\Omega^{4/3}}\left[\frac{1}{3}\ln\frac{\left[l_1^{(t)}-\left(\frac{V_p}{2\pi}\right)^{1/3}\right]\left[l_1^{(t)1/2}-\left(\frac{V_p}{2\pi}\right)^{1/6}\right]\left[l_1^{(t_0)1/2}+\left(\frac{V_p}{2\pi}\right)^{1/6}\right]}{\left[l_1^{(t_0)}-\left(\frac{V_p}{2\pi}\right)^{1/3}\right]\left[l_1^{(t_0)1/2}-\left(\frac{V_p}{2\pi}\right)^{1/6}\right]\left[l_1^{(t)1/2}+\left(\frac{V_p}{2\pi}\right)^{1/6}\right]}\right.$$
$$+\frac{1}{6}\ln\frac{\left[l_1^{(t_0)2}+l_1^{(t_0)}\left(\frac{V_p}{2\pi}\right)^{1/3}+\left(\frac{V_p}{2\pi}\right)^{2/3}\right]\left[l_1^{(t_0)}+l_1^{(t_0)1/2}\left(\frac{V_p}{2\pi}\right)^{1/6}+\left(\frac{V_p}{2\pi}\right)^{1/3}\right]\left[l_1^{(t)}-l_1^{(t)1/2}\left(\frac{V_p}{2\pi}\right)^{1/6}+\left(\frac{V_p}{2\pi}\right)^{1/3}\right]}{\left[l_1^{(t)2}+l_1^{(t)}\left(\frac{V_p}{2\pi}\right)^{1/3}+\left(\frac{V_p}{2\pi}\right)^{2/3}\right]\left[l_1^{(t)}+l_1^{(t)1/2}\left(\frac{V_p}{2\pi}\right)^{1/6}+\left(\frac{V_p}{2\pi}\right)^{1/3}\right]\left[l_1^{(t_0)}-l_1^{(t_0)1/2}\left(\frac{V_p}{2\pi}\right)^{1/6}+\left(\frac{V_p}{2\pi}\right)^{1/3}\right]}$$
$$+\left(\frac{1}{\sqrt{3}}\right)\left[\arctan\left\{\frac{1}{\sqrt{3}}\left[\left(\frac{16\pi}{V_p}\right)^{1/3}l_1^{(t_0)}+1\right]\right\}-\arctan\left\{\frac{1}{\sqrt{3}}\left[\left(\frac{16\pi}{V_p}\right)^{1/3}l_1^{(t)}+1\right]\right\}\right.$$
$$+\arctan\left(\frac{1}{\sqrt{3}}\left\{\left[\left(\frac{128\pi}{V_p}\right)^{1/3}l_1^{(t)}\right]^{1/2}+1\right\}\right)-\arctan\left(\frac{1}{\sqrt{3}}\left\{\left[\left(\frac{128\pi}{V_p}\right)^{1/3}l_1^{(t_0)}\right]^{1/2}+1\right\}\right)$$
$$\left.+\arctan\left(\frac{1}{\sqrt{3}}\left\{\left[\left(\frac{128\pi}{V_p}\right)^{1/3}l_1^{(t)}\right]^{1/2}-1\right\}\right)-\arctan\left(\frac{1}{\sqrt{3}}\left\{\left[\left(\frac{128\pi}{V_p}\right)^{1/3}l_1^{(t_0)}\right]^{1/2}-1\right\}\right)\right] \tag{24}$$

Eqs. (10) and (22) to evaluate $(\mathrm{d}R_a/\mathrm{d}t)_{\mathrm{StrCyl}}$ and $(\mathrm{d}R_a/\mathrm{d}t)_{\mathrm{StrCube}}$, respectively, yielding

$$\left(\frac{\mathrm{d}R_a}{\mathrm{d}t}\right)_{\mathrm{StrCube}} = -\frac{3}{2}\left(\frac{V_p}{8}\right)^{-1/3}\cdot R_a^{5/3}\left(\frac{\mathrm{d}l_1}{\mathrm{d}t}\right)_{\mathrm{StrCube}}$$
$$= 96\left(\frac{V_p^{4/3}D_s\gamma\Omega^{4/3}}{kT}\right)\cdot R_a^{5/3}\left(\frac{1-R_a}{1+R_a}\right) \tag{25a}$$

$$\left(\frac{\mathrm{d}R_a}{\mathrm{d}t}\right)_{\mathrm{StrCyl}} = -\frac{3}{2}\left(\frac{V_p}{2\pi}\right)^{-1/3}\cdot R_a^{5/3}\left(\frac{\mathrm{d}l_1}{\mathrm{d}t}\right)_{\mathrm{StrCyl}}$$
$$= 6(2\pi)^{4/3}\left(\frac{V_p^{4/3}D_s\gamma\Omega^{4/3}}{kT}\right)\cdot R_a^{5/3}\left(\frac{1-R_a}{1+R_a}\right) \tag{25b}$$

The $(\mathrm{d}R_a/\mathrm{d}t)_{\mathrm{StrCyl}}$:$(\mathrm{d}R_a/\mathrm{d}t)_{\mathrm{StrCube}}$ ratio is a constant, giving $\mathrm{d}t_{\mathrm{StrCyl}}/\mathrm{d}t_{\mathrm{StrCube}} = 16/(2\pi)^{4/3} = 1.380$. That this ratio is of the order of unity is consistent with the observations in the 2-D case;[4] the times for evolution are relatively insensitive to the detailed geometry of the evolving entity. Thus, even though cavities in a real material will not assume either of the shapes considered, a comparison of experimental results with these predictions should nonetheless be useful.

A key feature of the stretched cylinder geometry is that it is possible in this case to define the form that the potential must take such that the divergence of the surface flux is constant everywhere on a particular facet. As in the 2-D case, one solves for the form of the potential that leads to a continuous potential and gradient in the potential at the facet edge, and sets the mean potential on a facet equal to the value implied by its weighted mean curvature. Such an analysis then allows the gradient in potential at the facet edge, and thereby the mass arrival and shape adjustment rates to be compared with those given by the linearized potential approach.

The assessment of the potential variation on the circular and edge faces follows the method used in the companion paper.[4] The general form of the potential variation for the circular faces (1), and edge faces (2) is

$$\mu_s^{(1)}(r) = c_1 r^2 + c_2 r + c_3 \tag{26a}$$

$$\mu_s^{(2)}(z) = d_1 z^2 + d_2 z + d_3 \tag{26b}$$

where the center of the circular face is $r = 0$, and the center of the edge is taken as $z = 0$. Because of the symmetry about $r = 0$ and $z = 0$, the constants c_2 and d_2 must be zero. The constants c_3 and d_3 can be evaluated by integrating the expressions, and setting the mean potential on the surfaces equal to the value implied by the weighted mean curvature, Eq. (19). When D_s is assumed to be the same on all facets,[††] the slope is continuous at the facet edge ($r = l_2$, $z = \pm l_1$), allowing c_1 and d_1 to be related to one another. Finally, equality of the potential at the facet edge allows the final unknown to be defined. The resulting expressions for the chemical potentials are

$$\mu_s^{(1)} = 6\bar{V}\left[\frac{l_2\gamma_1 - l_1\gamma_2}{l_1 l_2(3l_2^2+4l_1l_2)}\right]\left[r^2 - \frac{l_2^2}{2}\right] + \mu_0 + \bar{V}\left[\frac{2\gamma_2}{l_2}\right] \tag{27a}$$

$$\mu_s^{(2)} = -6\bar{V}\left[\frac{l_2\gamma_1 - l_1\gamma_2}{l_1^2(3l_2^2+4l_1l_2)}\right]\left[z^2 - \frac{l_2^2}{3}\right] + \mu_0 + \bar{V}\left[\frac{\gamma_1}{l_1}+\frac{\gamma_2}{l_2}\right] \tag{27b}$$

The chemical potential gradient at the edge of the circular face can be evaluated, and compared with that obtained using the linearized potential approach with $\Delta x_{2\to1}$ set equal to $\frac{1}{2}(l_1 + l_2)$. Using Eq. (27), and evaluating $\mathrm{d}\mu_s^{(1)}/\mathrm{d}r$ at $r = l_2$ gives

$$\left(\frac{\mathrm{d}\mu_s^{(1)}}{\mathrm{d}r}\right)_{r=l_2}^{(\mathrm{pp})} = 3\bar{V}\left[\frac{l_2\gamma_1 - l_1\gamma_2}{l_1 l_2\left(l_1 + \frac{3}{4}l_2\right)}\right] \tag{28}$$

for the parabolic potential (pp). The equivalent result for the linearized potential (lp) approximation is

$$\left(\frac{\mathrm{d}\mu_s^{(1)}}{\mathrm{d}r}\right)_{r=l_2}^{(\mathrm{lp})} = -\frac{\Delta\bar{\mu}_{2\to1}}{\Delta x} = 2\bar{V}\left[\frac{l_2\gamma_1 - l_1\gamma_2}{l_1 l_2(l_1+l_2)}\right] \tag{29}$$

The ratio of the gradients thus depends upon the aspect ratio, and is given by

$$R_g = \frac{(\mathrm{d}\mu/\mathrm{d}r)_{\mathrm{lp}}}{(\mathrm{d}\mu/\mathrm{d}r)_{\mathrm{pp}}} = \frac{2\left(l_1 + \frac{3}{4}l_2\right)}{3(l_1+l_2)} = \frac{2}{3}\left[\frac{1+\frac{3}{4}R_a}{1+R_a}\right] \tag{30}$$

[††]Yu and Hackney[18] treated the shape relaxation of a 2-D rectangular particle for which the surface diffusivity was assumed to differ on the adjoining facets. In such cases, the flux at the facet edge must be balanced, and the gradient will change discontinuously at the facet junction.

When $R_a \rightarrow \infty$, $R_g \rightarrow \frac{1}{2}$, and the parabolic potential leads to an evolution rate that is a factor of 2 higher than the linearized potential. When $\gamma_1 = \gamma_2 = \gamma$, the equilibrium value of R_a is unity, and when $R_a \rightarrow 1$, $R_g \rightarrow 7/12$. It follows that the evolution times for the parabolic potential are of the order of one-half those predicted by the linearized potential. This disparity is similar to that seen in the 2-D cases,[4] and smaller than the uncertainty in the input parameters. We presume that the approximate equations describing the evolution of the stretched cube, Eqs. (12) and (13), will differ by a similarly small amount from that predicted by a more exact solution. Figure 5 compares the evolution times predicted by the three 3-D models.

III. Experimental Measurements of Pore Shape Changes

The ability to model pore shape changes, and the close agreement between the results obtained when using the linearized and continuous potential approaches to modeling, provided an incentive to perform experimental measurements of pore shape changes. The ability to produce arrays of nonequilibrium shape pores using microlithographic methods[5,13] was exploited.

Optical-finish (premium-grade) sapphire single-crystal substrates with (0001), $\{10\bar{1}2\}$, $\{11\bar{2}0\}$, and $\{10\bar{1}0\}$ orientations (abbreviated as **c**, **r**, **a**, and **m**, respectively) were purchased (Meller Optics, Providence, RI). The orientation of each sample was confirmed to be within $\pm 2°$ of the specified orientation through analysis of X-ray back reflection diffraction patterns (Laue method).

A chromium mask containing a square array (250 × 250) of pores individually 16 μm × 16 μm with a 16 μm edge-to-edge spacing was fabricated. Using this mask, 62 500 identical surface cavities with a final size of ≈20 μm × 20 μm × 0.5 μm were lithographically introduced onto **c**, **r**, **a**, and **m** orientation sapphire substrates 12.7 mm × 12.7 mm × 0.38 mm thick.

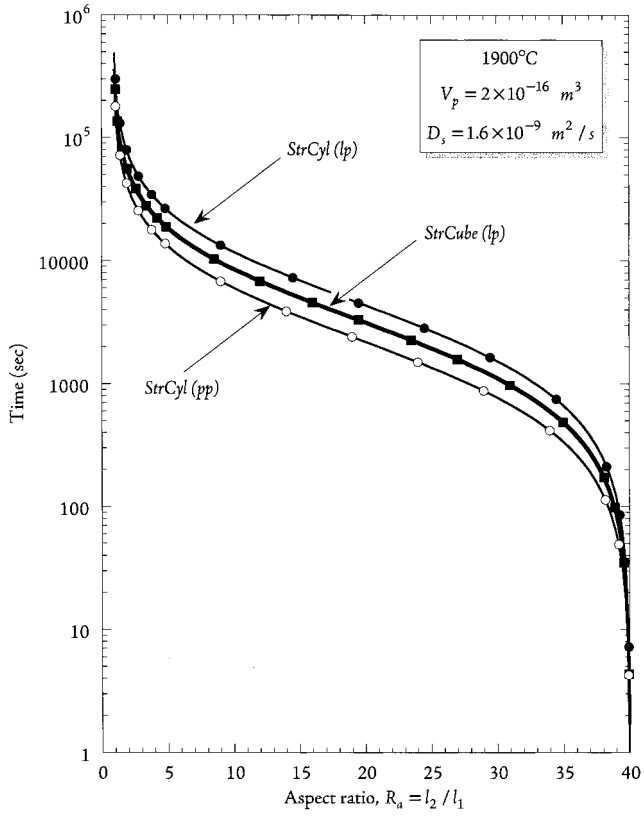

Fig. 5. Plot of evolution time versus aspect ratio comparing the predictions for a stretched cube using a linearized potential (*lp*), and the approximate (*lp*) and exact (*pp*) solutions for a stretched cylinder. The initial aspect ratio is chosen to be 40, and the volume is held fixed at 2×10^{-16} m^3 to match the experimental conditions.

A second substrate of identical orientation was placed upon the etched surface and aligned to produce, at worst, a very low angle misorientation (≤1°) twist boundary. The two sapphire substrates were bonded to one another in a graphite heating element, vacuum hot-press at 1300°C with an applied pressure of 9 MPa sustained for 1 h; the ambient gas pressure during bonding was $\approx 2.6 \times 10^{-3}$ Pa.[‡‡] Thin high-purity BN plates were placed between the assemblies and the graphite spacer to avoid reaction between them. Very little adjustment of the pore shape occurred during bonding.

The external surfaces of bonded assemblies were polished using 6-μm diamond paste to render the samples transparent for optical microscopy. Specimens were placed on a high-purity alumina block (99.997%) in an alumina crucible (99.7%) which was prebaked under vacuum ($<1.3 \times 10^{-3}$ Pa) at 1900°C for 20 h prior to usage to remove volatile impurities. Annealing was performed in a Mo mesh heating element furnace (Centorr) under vacuum ($<1.3 \times 10^{-3}$ Pa) at 1900°C. Samples were initially annealed for 4 h and then for an additional 12 h. The morphological evolution of pores was monitored using optical microscopy. The **m**-specimen was annealed for yet an additional 8 h, and then ground using a high-speed grinding wheel. The plane containing the pores was inclined slightly to the plane of grinding. This made it possible to expose a portion or strip of the pore array, while maintaining the other pores fully enclosed by sapphire. Grinding damage was removed by polishing using 1-μm diamond slurry on a 12-in.-diameter solder plate with a tripole specimen holder (Logitech, PM4). This polishing method causes much less damage to the pore edge than any other polishing methods examined, and made detailed observation of the pore shape possible. The pores exposed in this manner were examined using both a scanning electron microscope (ISI DSI30) and an atomic force microscope (Park Instrument) to identify the facet structure.

IV. Results and Discussion

Figures 6(a–e) show the morphological evolution of internal pores in sapphire substrates of various surface orientations in response to annealing at 1900°C. Figure 6(a) shows the initial ("as-bonded" pore array composed of ≈20 μm × 20 μm pores etched to a depth of ≈0.5 μm common to each sample. The pore shapes that develop on **c**-, **r**-, **a**-, and **m**-oriented substrates after total anneal times of 4 and 16 h at 1900°C, are shown in Figures 6(b–e), respectively. It is evident that the substrate orientation, and thus the crystallography of the surface that dominates the initial pore shape, has a profound effect on the rate and nature of the morphological evolution.

Of the orientations examined, the **m**-orientation specimen evolved most rapidly and homogeneously. A bright region in an optical micrograph of a pore indicates the presence of a plane perpendicular to the incoming light, and thus parallel to the original substrate surface. The disappearance of this bright spot is taken as an indication that the original substrate surface has disappeared, and is thus unstable. The **m**-plane appears to disappear within the first 4 h of annealing. In contrast, for the **c**-orientation substrate, there was minimal morphological change even after 16 h at 1900°C. The **r**- and **a**-orientation specimens

[‡‡]One potential drawback of studying internal voids produced by this method is that one is unsure of the atmosphere in contact with the pore surfaces. The two bonding surfaces are placed in contact in an air environment, and thus, air should be present in the cavities. A pressure is applied to the two substrates to bring them into close contact, and to establish good alignment of the specimens. The seal is not hermetic, and thus, one expects that the air inside at least some of the surface cavities escapes during pumpdown of the hot-press, during heating and prior to complete bonding (sealing) of the interface. At least some of the pores might be expected to have an internal atmosphere dictated by the hot-pressing environment (vacuum, graphite die) at the time the pore is sealed. If the gas composition was a variable, and it caused important differences in the behavior, differences between the behavior of cavities nearer the sample edge (and more likely to be evacuated) and those in the center of the sample might be expected. No such differences have been observed. However, we must acknowledge the possibility that the composition of the gas within our pores may differ from that in other experiments[3] where crack healing in air is used to produce pores.

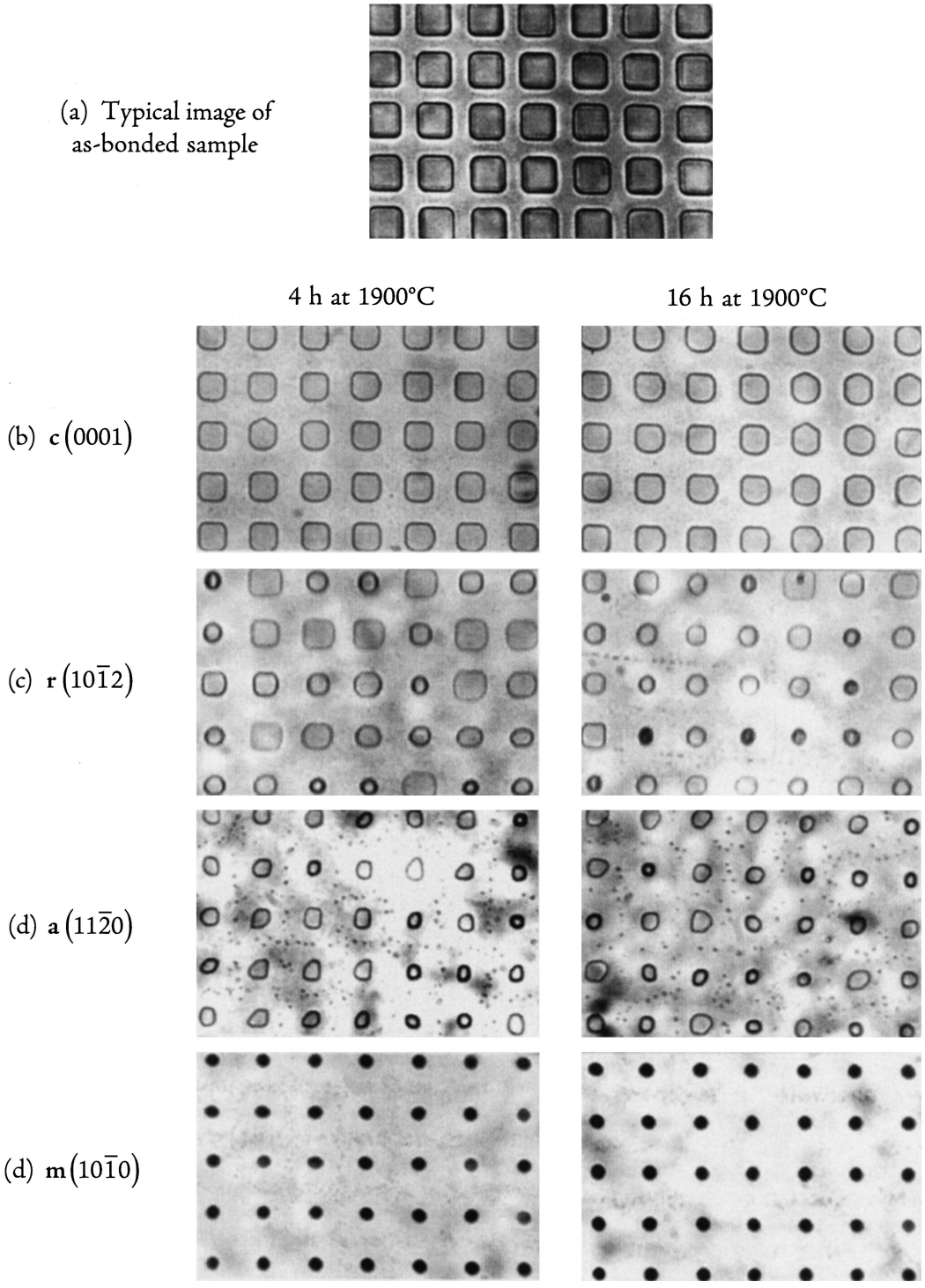

Fig. 6. Optical micrographs of internal pores in sapphire of varying orientation: (a) after bonding, but prior to annealing, and (b–e) after anneals of 4 and 16 h at 1900°C for samples of the indicated surface orientations.

showed intermediate "average" rates of evolution, but the evolution is inhomogeneous. A region of bright contrast persisted in both **r**- and **a**-orientation specimens, even after 16 h at 1900°C. Collectively, these observations suggest that the **c**-, **r**-, and **a**-planes are low-energy surfaces and part of the Wulff shape of undoped alumina; the rapid disappearance of the **m**-plane suggests that it is not a component of the equilibrium shape.

The pore shape in the **m**-oriented specimen appeared to be closest to being equilibrated after 4 h at 1900°C; no significant change in the morphology was apparent when the annealing time was increased from 4 to 16 h. Figure 7 shows an SEM micrograph of an exposed ribbon of pores, and a higher magnification micrograph of the pore shape on an **m**-oriented substrate after 24 h at 1900°C. Several facets are evident; the **c**- and **a**-facets which are perpendicular to the **m**-plane intersect the plane of polish. Figure 8 shows the results of an AFM line scan used to confirm that facets observed inside the pore correspond to **r**- and **a**-planes. The **m**-oriented specimen was also cut perpendicular to the **c**-orientation. Figure 9 is an SEM micrograph of the pore shape as viewed along the [0001] direction; the plane at the base of the pore is a **c**-plane. The pore morphology provides further evidence that the **c**-, **r**-, and **a**-planes are components of the Wulff shape of alumina, while the **m**-plane is not. It also indicates that 24 h at 1900°C is insufficient to achieve an equilibrium shape. Since alumina has rhombohedral

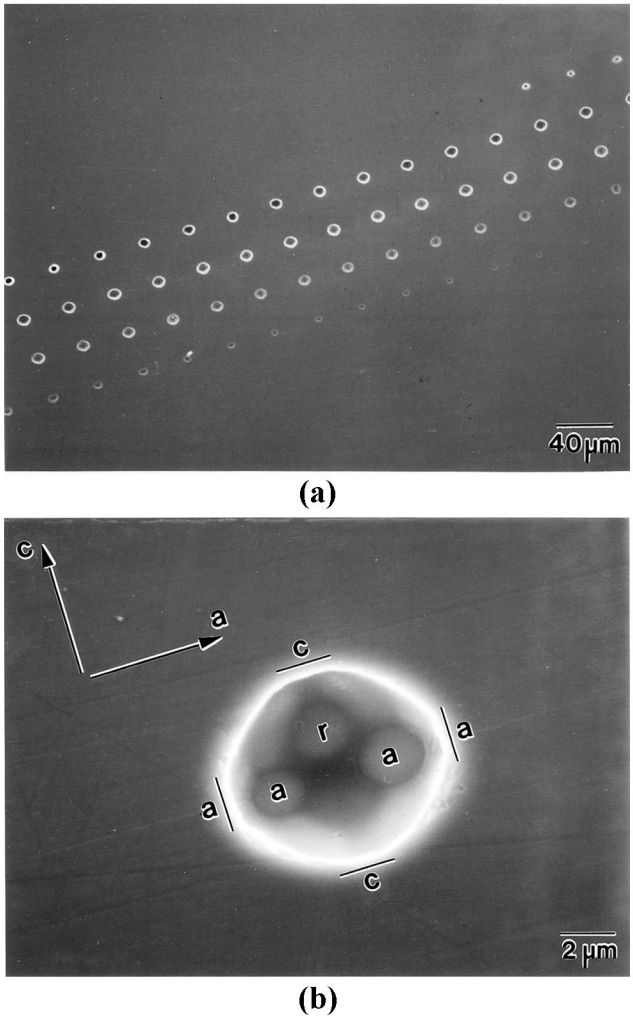

Fig. 7. (a) Lower-magnification SEM micrograph of a strip of pores, part of a larger array etched into an **m**-plane substrate, and exposed by polishing after 24 h anneal at 1900°C. (b) Higher-magnification SEM micrograph of an individual pore showing that **c**-, **r**-, and **a**-type facets have formed during annealing.

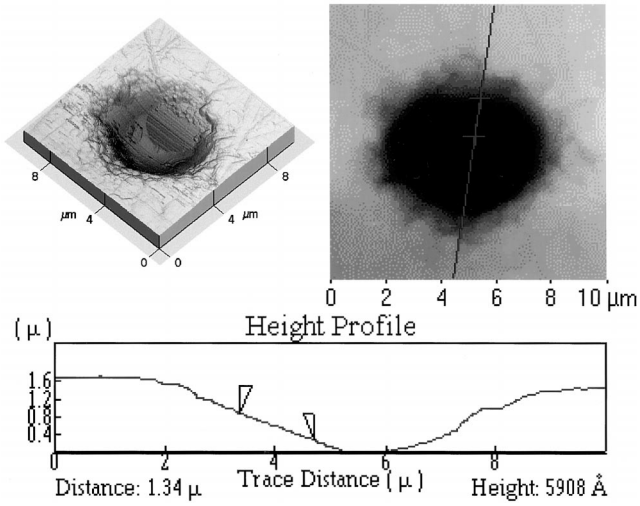

Fig. 8. Illustration of the use of AFM to determine the inclination angles made by facets within pores with respect to the surface of known orientation and known directions within this plane. The pores were originally etched into the **m**-plane and annealed for 24 h at 1900°C. Both **r**- and **a**-facets were identified from the inclination angles.

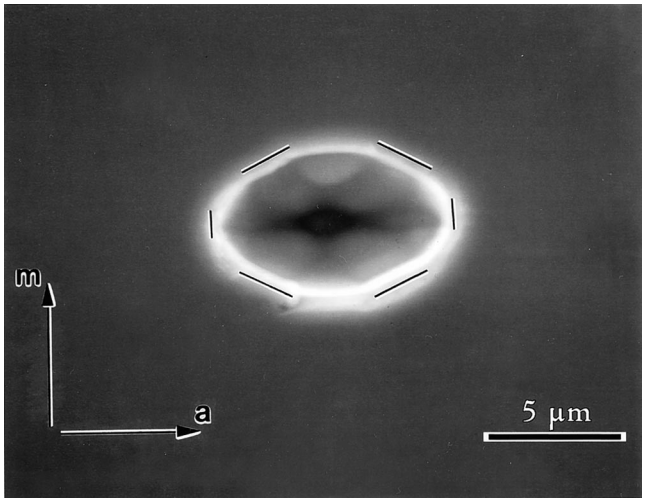

Fig. 9. SEM micrograph of pore etched into the **m**-plane, but sectioned and viewed along the **c**-direction after 24 h annealing at 1900°C. The six lines correspond to the orientation of the **a**-planes, and the central facet is a **c**-facet. It is evident that the pore does not yet have the symmetry of an equilibrated pore.

symmetry, six identical **a**-facets should be observed, and there should be 3-fold symmetry along the **c**-direction. However, two of the six **a**-facets intersecting the plane of polish are much smaller than the other four, and the 3-fold symmetry is missing. One possible explanation of the observations is that the **m**-plane quickly decomposed into **r**- and **a**-planes, and once the **m**-plane was consumed, the evolution rate decreased substantially.

The significant differences in evolution rates among the various samples (orientations) examined could indicate that $\delta_s D_s$ varies substantially with surface orientation, or that mass transport on stable low-index planes of alumina is controlled by SALK. To examine the latter hypothesis, pore evolution rates for the different orientation surfaces were compared with the results predicted for diffusion control by the 3-D "stretched cube" analysis presented earlier. In order to encompass the full (and very wide) range of surface diffusivities in the literature, values of D_s corresponding to the highest, average, and lowest values for nominally pure alumina,[19] 1.23×10^{-7}, 1.60×10^{-9}, and 2.92×10^{-10} m^2/s, respectively, at 1900°C, surface energy, $\gamma_1 \approx \gamma_2 = 1.0$ J/m^2, and effective molecular volume, $\Omega = 2.11 \times 10^{-29}$ m^3, were used as input parameters for the simulations. The initial pore geometry in the simulation was adjusted to conform to the current experimental conditions.

Before we compare the results and predictions, several difficulties and limitations to such a comparison should be noted. Although the geometric parameters that define the *initial* pore geometry can be adjusted to conform to the current experimental conditions, the actual facet structure of the pores differs from that in the simulation, as is evident in Figs. 7–9. The 2-D analyses presented previously[4] show that the cavity size and temperature primarily affect the evolution times; the details of the initial cavity shape and the nature of the ultimate equilibrium shape have only a modest effect. The 3-D analyses for the stretched cube and stretched cylinder in this paper similarly suggest that when the initial cavity geometry is very far from equilibrium, and the evolution times of cavities of identical volume but different shape are compared, the shape effects are relatively minor. We assume that the same holds in the present case. In contrast, changes in the rate-controlling mechanism may produce very large effects.

The width of 20 representative pores (out of 62 500) was measured from a photograph for each specimen, and the l_2/l_1 ($=w/d$) ratio was calculated. The projected area of the pore was approximated as a square cross section of equivalent area when viewed perpendicular to the bonding plane. The edge length of the square, w, was calculated. The cavity depth d was calculated by assuming that the pore volume was conserved. Figure 10 compares the results of these measurements with the predictions of the

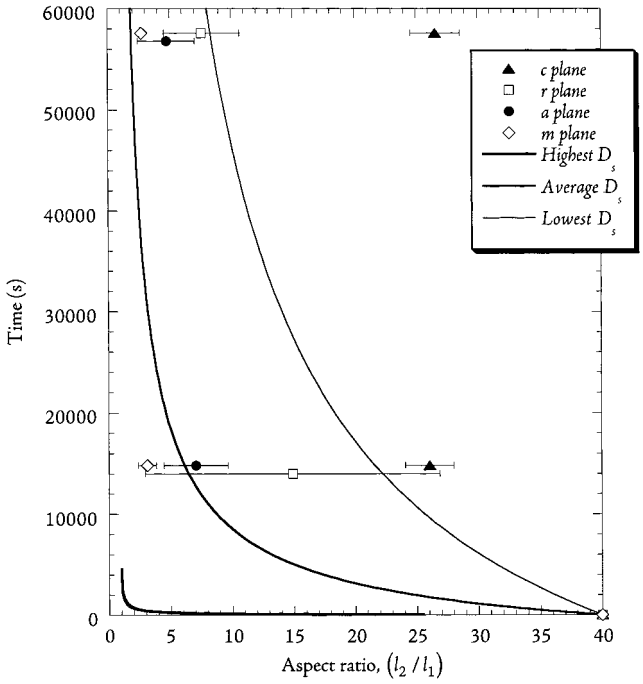

Fig. 10. Plot of computed times to reach specific l_2/l_1 ratios at 1900°C as a function of $\delta_s D_s$, and comparison with experimental data. (Selected data points are shifted slightly on the time axis to allow better resolution of the error bars; all data are at 4 and 16 h.) The predictions are for a stretched cube, as described by Eq. (13).

simulation. Error bars indicate standard deviations for each set of measurements.

It is clear that if one insists on an interpretation of the results in terms of surface-diffusion-controlled evolution $\delta_s D_s$ would have to vary substantially with surface orientation. Moreover, to rationalize the observed time dependence of the l_2/l_1 ratios would require a diffusivity that decreases with time. Regardless of the substrate orientation, the experimental pore shape trajectories cross those derived for a constant D_s. This is particularly noticeable for the **c**-oriented substrate; the l_2/l_1 ratio evolves from 40 to ≈26 during the first 4 h, and then appears essentially unchanged during further annealing. For the **m**-oriented substrates, the l_2/l_1 ratio evolves from 40 to ≈3 during the first 4 h, and from ≈3 to ≈2.7 during an additional 12 h of annealing. From the standpoint of kinetics, the morphological evolution is nearly completed in the first 4 h of annealing even though from an energetic point of view the shapes remain far from equilibrium,[2,3] and a driving force for mass transport still exists.

An alternative, and we believe, more plausible explanation of the observations is that the process is diffusion-controlled only during the very initial stages of evolution (possibly for anneals <4 h for some orientations), and gives way to SALK-dominated behavior in the later stages. The classic work of Burton, Cabrerra, and Frank[20] on the growth of facetted crystals pointed out that the motion of a facet will require the nucleation and growth of atomic height patches on an advancing surface, and addressed the role that screw dislocations could have on facilitating facet motion. Willertz and Shewmon[21] addressed this nucleation problem in an effort to rationalize the sluggish migration rates of helium-filled voids in gold and copper foils. They concluded that the nucleation of steps on a facetted surface could limit the migration rate, and account for bubble velocities that were lower than expected from an analysis assuming surface-diffusion-controlled migration. More recently, Mullins and Rohrer[22] treated the nucleation problem in the context of volume-conserving shape changes of facetted crystals. Their results suggest that for facets larger than ≈1 nm in size, nucleation of a new facet layer will limit the evolution rate unless the facet is intersected by a dislocation. The same issues are relevant in interpreting the results of the present experiments.

Lithography provides the opportunity to systematically assess the sensitivity of the observed behavior to the orientation of the sapphire substrate. A major factor affecting the kinetics is believed to be the stability of the surface that dominates the as-bonded pore shape. Both the results of Choi *et al.*[3] at 1600°C and the studies of Kitayama[2,14] at 1600° and 1800°C have shown that the **c** (0001), **r** $\{10\bar{1}2\}$, and **a** $\{11\bar{2}0\}$ planes are part of the Wulff shape of undoped sapphire. The presence/formation of **c**-, **r**-, and **a**-orientation facets in cavities originally etched into the **m**-plane (Figs. 7 and 9) suggests that these surfaces remain part of the Wulff shape at 1900°C. If this is the case, then when cavities are etched into **c**-, **r**-, and **a**-orientation substrates, the dominant bounding surfaces of the etched-in pore are stable. These bounding surfaces are likely to contain irregularities or defects due to nonuniform ion beam etching and polishing scratches, and a terrace-and-step structure may evolve due to small miscuts of the wafer with respect to the ideal orientation. These surface defects (steps) will provide sources and sinks for adatoms during the initial stages of evolution.

For such vicinal surfaces, the morphological evolution will reflect the dynamics of surface steps. During annealing, perturbations in the stable surface will have a driving force to decay. Duport *et al.*[23,24] have considered the role of critical fluctuations in a related problem, the decay of grooves cut into a surface with singular orientation. In this case, profile decay requires the development of sufficiently large fluctuations in the topmost layer to form isolated loops or patches of atoms on a stable facet. The shrinkage of this loop, and peeling off of atoms from the topmost layer, lead to profile decay. This process is slow in comparison to diffusion-controlled decay. Surnev *et al.*[25] have performed elegant experiments in which a periodic surface profile was etched into a Au(111) vicinal surface and the profile decay was monitored. It was shown that varying the profile orientation with respect to the step direction on the surface resulted in significantly different decay kinetics. A discussion of the role of atomic steps and the miscut in the evolution of periodic surface modulations can be found in the review by Blakely *et al.*[26]

For nonequilibrium shape cavities introduced into **c**-, **r**-, and **a**-orientation substrates one can then expect that three processes with different spatial and temporal characteristics will be active. At a spatial scale smaller than the dimensions of the large ≈20 μm × 20 μm facet, there will be a driving force to "smooth" any perturbations that may exist, and this will reduce the spatial density of ledges and kinks. When considering profile decay on a macroscopic sample, eliminating the ledge structure due to a miscut would require long-range mass transport, and thus, the ledge structure persists. In the present case, migration of ledges over distances less than or equal to the pore dimension would reorient the surface, and eliminate the ledge structure due to a miscut. Once flat and stable facets are formed, adjusting the aspect ratio of the pore requires the nucleation of patches of adatoms on surfaces that must advance toward the pore center, and the nucleation of critical size cavities in surfaces that must recede from the pore center as the equilibrium shape is approached. These nucleation processes are likely to occur at a low and declining rate as the driving force for morphological change decreases.

Heffelfinger *et al.*[27] have recently examined the evolution of surface structure on (0001) α-alumina single crystals by annealing vicinal single crystals at 1400°C for varying periods of time and characterizing the surface using AFM. The results indicate that during the early stages of evolution (10 min), steps of height $c/6$ (≈0.2 nm) develop. With further annealing (≤8 h), bunching of these steps occurs, leading to the formation of steps of height c or multiples of c. The facet junction density decreases substantially during the first few hours of annealing at 1400°C.[28] These observations suggest that at 1900°C step-bunching should be complete in a very short time. As a result, in the absence of some other source of ledges and steps, the aforementioned nucleation and growth processes would be necessary for further evolution. This scenario is consistent with the general trend of an apparent surface diffusivity that is decreasing with increasing anneal time, and would explain the behavior of pores etched into **c**-orientation

substrates particularly well. The apparent D_s for pores etched into the **c**-orientation substrates ultimately falls below even the lowest estimate of D_s at 1900°C.[§§]

Pore shape evolution in **r**- and **a**-oriented specimens is inhomogeneous. Slowly evolving pores may be subject to the same nucleation process described before; the more rapidly evolving pores may benefit from a structural defect that provides a source of steps. Lemaire and Bowen examined the migration of gas-filled pores in KCl due to an imposed temperature gradient.[29] For small pores, $\leq$50 μm, a size-dependent probability of motion was observed; pores greater than ≈50 μm in width were always mobile. Olander *et al.*[30] examined the migration of liquid-filled inclusions in KCl and NaCl single crystals, and found that inclusions smaller than 10 μm in width were essentially immobile. In both cases, these behaviors were explained by relating the rate of mass removal/addition to the density of dislocation intersections with the facetted cavities/inclusions. (In the work of Willertz and Shewmon,[21] the cavities were <0.1 μm in radius.) The extension of these results to the present case would suggest that the more rapidly evolving pores observed in **r**- and **a**-oriented specimens are intersected by a larger number of dislocations, and thus have a higher step density. Those cavities that evolve more slowly would have fewer (or no) dislocation intersections. Dislocation densities were not measured as part of this study, and would most likely be altered by the bonding process. However, a dislocation density of $2.5 \times 10^5/\text{cm}^2$ would be required to have an average of one dislocation intersecting each 20 μm × 20 μm face. If the dislocation density is of this order, substantial variations in evolution rates could be expected due to statistical variations in the number of intersections.[¶¶] As the l_2/l_1 ratio decreases, and the projected pore area decreases, so also does the probability of intersecting a dislocation. One can then anticipate that if a pore separates from an intersecting dislocation, the evolution rate will decrease. (If this correctly explains the observations involving stable planes, then it would imply either that the dislocation intersection density in **c**-oriented samples is much lower or that some other process limits the evolution rate in these samples.)

Pore shape evolution in **m**-oriented substrates was rapid and uniform. The apparent $\delta_s D_s$ during the early stages of evolution exceeded the average value at this temperature, and then decreased with increasing anneal time. The results of Choi *et al.*[3] and the studies of Kitayama[2,14] demonstrate that the **m** $\{10\bar{1}0\}$ plane is not part of the Wulff shape of undoped sapphire between 1600° and 1800°C. Observations by Heffelfinger *et al.*[28,32] indicate that the **m** $\{10\bar{1}0\}$ plane decomposes into a fine spatial scale hill-and-valley structure comprised of other low-index planes at 1400°C. Experiments by Marks[33] have confirmed these 1400°C observations, and shown that the hill-and-valley structure persists during anneals at 1600°C. Similar changes at 1900°C would lead to structural disruption of the dominant bounding plane.

The detailed AFM studies by Heffelfinger and Carter[28] indicate that decomposition of the **m** $\{10\bar{1}0\}$ plane involves the nucleation of individual facets. These facets facilitate the nucleation of additional adjacent facets, causing the formation of packets of facets. The impingement of facet colonies that are out of phase leads to facet junction formation. One infers from the present study that this hill-and-valley structure facilitates rapid evolution of the pore shape. Initially, facet junction motion,[28] a higher facet layer nucleation rate on nanometer-scale facets,[22] and a higher dislocation intersection density may all contribute to the high evolution rate. However, the facet junction density decreases rapidly at 1400°C,[28] and a more rapid decrease would occur at 1900°C, contributing at least in part to the rapid decrease in evolution rate. The observed evolution rate decrease may also partly be due to the development of larger stable facets whose motion is nucleation limited as the pore approaches its equilibrium shape.

[§§]It is interesting to note that the void migration rates observed in gold and copper foils[21] implied surface diffusivities that were 10^{-4}–10^{-5} and 10^{-1}–10^{-2} times those measured by independent means for gold and copper, respectively.

[¶¶]Mader and Rühle[31] have reported a dislocation density of $\leq 10^4/\text{cm}^2$ in unbonded sapphire wafers.

V. Summary

The shape evolution kinetics of an idealized, completely facetted, isolated crystal/pore by surface diffusion have been modeled. The modeling approach extends that applied previously to 2-D geometries.[4] As was the case for the 2-D geometries, the details of the crystal/pore shape do not have a major impact on the predicted behavior provided that the shapes remain far from the equilibrium shape. When the crystal/pore volume is fixed, and the initial aspect ratio is the same, factor of 2 differences in evolution time owing to shape differences are suggested. The approximations made in modeling the potential gradient appear to also introduce roughly factor of 2 errors, and predict more sluggish evolution than models[1,3] that specify the spatial dependence of the surface potential.

Experimental studies were performed in which lithography was used to introduce arrays of nonequilibrium shape pores into sapphire substrates with known orientations. During high-temperature annealing (1900°C), pore shape evolution rates varied significantly with the orientation of the sapphire. The most rapid evolution occurs when the surface is unstable and is expected to evolve into a hill-and-valley structure. In this case, the surface may be macroscopically planar, but rough on a microscopic scale, thereby providing a high density of sites at which mass addition or removal occurs readily. For evolution of pores etched into stable low-index surfaces of alumina, interpreting the results in the context of a surface-diffusion-controlled process yields widely varying and time-dependent values of the apparent surface diffusivity. Comparison of the experimental results with the predictions of the modeling work suggests that SALK plays an important role in surface mass transport on stable low-index surfaces of alumina.

Acknowledgments

One of the authors (A.M.G.) would like to express gratitude to Professor W. W. Mullins, Professor C. B. Carter, and Professor A. W. Searcy for several useful conversations relating to the topic of pore shape evolution in facetted systems. We thank Professor G. S. Rohrer for providing an advance copy of Ref. 22 and Professor P. G. Shewmon for making us aware of Ref. 21. We would also like to thank the outstanding staff of the Microfabrication Laboratory at the University of California at Berkeley for helping to make the experimental component of this research possible.

References

[1]W. C. Carter, A. R. Roosen, J. W. Cahn, and J. E. Taylor, "Shape Evolution by Surface Diffusion and Surface Attachment Limited Kinetics on Completely Facetted Surfaces," *Acta Metall. Mater.*, **43** [12] 4309–23 (1995).

[2]M. Kitayama, "The Wulff Shape of Doped and Undoped Sapphire"; Ph.D. Thesis. Department of Materials Science and Mineral Engineering, University of California, Berkeley, CA, December 1996.

[3]J. Choi, D. Kim, B. J. Hockey, S. M. Wiederhorn, C. A. Handwerker, J. E. Blendell, W. C. Carter, and A. R. Roosen, "The Equilibrium Shape of Internal Cavities in Sapphire," *J. Am. Ceram. Soc.*, **80** [1] 62–68 (1997).

[4]M. Kitayama, T. Narushima, W. C. Carter, R. M. Cannon, and A. M. Glaeser, "The Wulff Shape of Alumina: I, Modeling the Kinetics of Morphological Evolution," *J. Am. Ceram. Soc.*, **83** [10] 2561–71 (2000).

[5]J. Rödel and A. M. Glaeser, "Microdesigned Interfaces: New Opportunities for Materials Science," *Yogyo Kyokaishi*, **99** [4] 251–65 (1991).

[6]J. Rödel and A. M. Glaeser, "High-Temperature Healing of Lithographically Introduced Cracks in Sapphire," *J. Am. Ceram. Soc.*, **73** [3] 592–601 (1990).

[7]J. D. Powers and A. M. Glaeser, "High-Temperature Healing of Cracklike Flaws in Mg- and Ca-Ion-Implanted Sapphire," *J. Am. Ceram. Soc.*, **75** [9] 2547–58 (1992).

[8]J. D. Powers and A. M. Glaeser, "High-Temperature Healing of Cracklike Flaws in Titanium Ion-Implanted Sapphire," *J. Am. Ceram. Soc.*, **76** [9] 2225–34 (1993).

[9]L. Kulinsky, J. D. Powers, and A. M. Glaeser, "Morphological Evolution of Pre-perturbed Pore Channels in Sapphire," *Acta Mater.*, **44** [10] 4115–30 (1996).

[10]J. Rödel and A. M. Glaeser, "Pore Drag and Pore-Boundary Separation in Alumina," *J. Am. Ceram. Soc.*, **73** [11] 3302–12 (1990).

[11]J. Rödel and A. M. Glaeser, "Anisotropy of Grain Growth in Alumina," *J. Am. Ceram. Soc.*, **73** [11] 3292–301 (1990).

[12]J. D. Powers and A. M. Glaeser, "Titanium Effects on Sintering and Grain Boundary Mobility of Alumina," *Ceram. Eng. Sci. Proc.*, **18** [4] 617–23 (1997).

[13]J. Rödel and A. M. Glaeser, "A Technique for Investigating the Elimination and Coarsening of Model Pore Arrays," *Mater. Lett.*, **6** [10] 351–55 (1988).

[14]M. Kitayama and A. M. Glaeser, "The Wulff Shape of Alumina: III, Undoped Alumina," unpublished work.

[15]M. Kitayama and A. M. Glaeser, "The Wulff Shape of Alumina: IV, Ti(IV)-Doped Alumina," unpublished work.
[16]M. Kitayama and A. M. Glaeser, "The Wulff Shape of Alumina: V, Mg, Ca, and Ti(III)-Doped Alumina," unpublished work.
[17]J. E. Taylor, "Overview No. 98 II—Mean Curvature and Weighted Mean Curvature," *Acta Metall. Mater*., **40** [7] 1475–85 (1992).
[18]S. H. Yu and S. A. Hackney, "On the Shape Change of a Nonequilibrium Faceted Microcrystal," *Scr. Metall. Mater*., **24** [11] 2077–82 (1990).
[19]T. K. Gupta, "Instability of Cylindrical Voids in Alumina," *J. Am. Ceram. Soc*., **61** [5–6] 191–95 (1978).
[20]W. K. Burton, N. Cabrera, and F. C. Frank, "The Growth of Crystals and the Equilibrium Structure of Their Surfaces," *Philos. Trans. R. Soc. London*, **243** [866] 299–358 (1951).
[21]L. E. Willertz and P. G. Shewmon, "Diffusion of Helium Gas Bubbles in Gold and Copper Foils," *Metall. Trans*., **1** [8] 2217–23 (1970).
[22]W. W. Mullins and G. S. Rohrer, "Nucleation Barrier for Volume-Conserving Shape Changes of Faceted Crystals," *J. Am. Ceram. Soc*., **83** [1] 214–16 (2000).
[23]C. Duport, A. Chame, W. W. Mullins, and J. Villain, "Decay of Grooves Cut in a Surface with Singular Orientation When the Neighboring Orientations are Unstable," *J. Phys. I: Gen. Phys., Stat. Phys., Condens. Matter, Cross-Disciplinary Phys.*, **6** [8] 1095–125 (1996).
[24]C. Duport, A. Chame, W. W. Mullins, and J. Villain, "Smoothing of a Grooved Singular Surface Whose Neighboring Orientations are Unstable"; pp. 71–81 in *Dynamics of Crystal Surfaces and Interfaces*. Edited by P. M. Duxbury and T. J. Pence. Plenum Press, New York, 1997.
[25]S. Surnev, B. Voigtlander, H. P. Bonzel, and W. W. Mullins, "Anisotropic Profile Decay on Perturbed Au(111) Vicinal Surfaces," *Surf. Sci*., **360** [1–3] 242–48 (1996).
[26]J. Blakely, C. Umbach, and S. Tanaka, "Atomic Steps in the Decay of 1- and 2-Dimensional Gratings"; pp. 23–39 in *Dynamics of Crystal Surfaces and Interfaces*. Edited by P. M. Duxbury and T. J. Pence. Plenum Press, New York, 1997.
[27]J. R. Heffelfinger, M. W. Bench, and C. B. Carter, "Steps and the Structure of the (0001) α-Alumina Surface," *Surf. Sci*., **370** [1] L168–72 (1997).
[28]J. R. Heffelfinger and C. B. Carter, "Mechanisms of Surface Faceting and Coarsening," *Surf. Sci*., **389** [1–3] 188–200 (1997).
[29]P. J. Lemaire and H. K. Bowen, "Migration of Small Pores in Potassium Chloride Due to a Temperature Gradient," *J. Am. Ceram. Soc*., **65** [1] 49–52 (1982).
[30]D. R. Olander, A. J. Machiels, M. Balooch, and S. K. Yagnik, "Thermal Gradient Migration of Brine Inclusions in Synthetic Alkali Halide Single Crystals," *J. Appl. Phys*., **53** [1] 669–81 (1982).
[31]W. Mader and M. Ruhle, "Electron Microscopy Studies of Defects at Diffusion-Bonded Nb/Al_2O_3 Interfaces," *Acta Metall*., **37** [3] 853–66 (1989).
[32]J. R. Heffelfinger, M. W. Bench, and C. B. Carter, "On the Faceting of Ceramic Surfaces," *Surf. Sci*., **343** [1–2] L1161–66 (1995).
[33]R. A. Marks, Department of Materials Science and Engineering, University of California, unpublished research, 1999. □